The Astrophysical Journal Supplement Series, 284:25 (14pp), 2026 May https://doi.org/10.3847/1538-4365/ae5655

NICER Magnetar Burst Catalog

Che-Yen Chu[1], Chin-Ping Hu[1], Teruaki Enoto[2,3], George A. Younes[4,5], Rachael Stewart[6], Zaven Arzoumanian[5], Wynn C. G. Ho[7], Zorawar Wadiasingh[5,8,9], Andrea Sanna[10], Sebastien Guillot[11], Gaurava K. Jaisawal[12], Matthew G. Baring[13], Marlon L. Bause[14], Tolga Güver[15,16], Chryssa Kouveliotou[6], Alex Van Kooten[6], and Keith C. Gendreau[5]

[1] Department of Physics, National Changhua University of Education, Changhua 500207, Taiwan; cychu@gapp.nthu.edu.tw, cphu0821@gm.ncue.edu.tw
[2] Department of Physics, Kyoto University, Kitashirakawa Oiwake, Sakyo, Kyoto 606-8502, Japan
[3] RIKEN Center for Advanced Photonics (RAP), 2-1 Hirosawa, Wako, Saitama 351-0198, Japan
[4] Center for Space Sciences and Technology, University of Maryland, Baltimore County, Baltimore, MD 21250, USA
[5] Astrophysics Science Division, NASA GSFC, 8800 Greenbelt Road, Greenbelt, MD 20771, USA
[6] Department of Physics, The George Washington University, Washington, DC 20052, USA
[7] Department of Physics and Astronomy, Haverford College, 370 Lancaster Avenue, Haverford, PA 19041, USA
[8] Department of Astronomy, University of Maryland, College Park, MD 20742, USA
[9] Center for Research and Exploration in Space Science and Technology, NASA/GSFC, Greenbelt, MD 20771, USA
[10] University of Cagliari, 09042, Monserrato, Sardinia, Italy
[11] Institut de Recherche en Astrophysique et Planétologie, UPS-OMP, CNRS, CNES, 9 avenue du Colonel Roche, BP 44346, Toulouse Cedex 4, 31028, France
[12] DTU Space, Technical University of Denmark, Ørsteds Plads 348, DK-2800 Lyngby, Denmark
[13] Department of Physics and Astronomy—MS 108, Rice University, 6100 Main Street, Houston, TX 77251-1892, USA
[14] Max Planck Institut für Radioastronomie, Auf dem Hügel 69, 53121 Bonn, Germany
[15] Istanbul University, Science Faculty, Department of Astronomy and Space Sciences, Beyazit, 34119, Istanbul, Türkiye
[16] Istanbul University Observatory Research and Application Center, Istanbul University, 34119, Istanbul, Türkiye
Received 2025 December 26; revised 2026 March 11; accepted 2026 March 20; published 2026 May 4

Abstract

In this paper, we present a comprehensive catalog of short bursts from magnetars based on 8 yr of NICER observations. A total of 1130 bursts were identified from 14 sources, with the sample dominated by SGR 1935+2154, which accounts for 76% of all detected bursts. We analyzed burst durations, spectral properties, and their correlations across multiple sources. Bursts from SGR 1935+2154 exhibit significantly longer durations, with a mean of 317 ms, compared to a mean of 23 ms for bursts from other magnetars. Two microsecond-scale bursts were detected for the first time, originating from 1E 1048.1−5937 and CXOU J010043.1−721134. Spectral analysis in the 0.5–8 keV range using both blackbody and power-law models shows that bursts with higher fluences have harder spectra. In contrast, correlations between burst duration and spectral parameters are weak or absent. This catalog provides a valuable dataset for studying magnetar short bursts, enabling future modeling efforts and improving our understanding of the diversity and physical mechanisms of magnetar bursts.

Unified Astronomy Thesaurus concepts: Neutron stars (1108); Magnetars (992); Soft gamma-ray repeaters (1471); X-ray bursts (1814); X-ray telescopes (1825); Catalogs (205); X-ray transient sources (1852)

Materials only available in the online version of record: machine-readable table

1. Introduction

Magnetars are a class of neutron stars characterized by their extremely strong magnetic fields, often on the order of 10^{14}–10^{15} G (R. C. Duncan & C. Thompson 1992; B. Paczynski 1992; P. Meszaros 1992). In the X-ray band, unlike rotation-powered pulsars, which typically show steady emission, magnetars are known for their highly variable and transient behavior (e.g., F. Coti Zelati et al. 2018). The first discovered magnetar burst was the giant flare from SGR 0526−66 in 1979, with a duration of about 10 minutes (E. P. Mazets et al. 1979b). Shortly afterwards, a series of short bursts, with durations ranging from milliseconds to seconds, was detected from SGR 1900+14 (E. P. Mazets et al. 1979a). Because these repeating events are dominated by emission in the soft γ-ray band, the sources were named soft gamma repeaters (SGRs). During a magnetar outburst, which can last from several months to several years, short bursts often appear in clusters known as burst forests or burst storms, with rates that can reach hundreds of bursts per hour (e.g., G. Younes et al. 2020; C.-P. Hu et al. 2025). In contrast, during the quiescent state, bursts may appear individually (e.g., F. P. Gavriil et al. 2002). According to the magnetar model, these bursts are generally thought to be triggered by activity in the neutron star crust, induced by extreme magnetic stresses (E. P. Liang & S. K. Antiochos 1984; R. C. Duncan & C. Thompson 1992; C. Thompson & R. C. Duncan 1995).

With the discovery of more SGRs, several short-burst catalogs of individual sources have been reported, including SGR 1806−20, SGR 1900+14, 1E 1547.0−5408, and SGR 0501+4516, etc. (E. Göğüş et al. 2001; A. J. van der Horst et al. 2012; L. Lin et al. 2013). Most of these studies focused on bursts in the hard X-ray band (>10 keV), while some extended to the soft X-ray range (<10 keV). The burst durations are typically log-normally distributed over more than 2 orders of magnitude, peaking around 200 ms. A clear correlation between spectral hardness and brightness has been observed in these catalogs, where bursts with higher fluence tend to exhibit harder spectra, regardless of the adopted spectral model (E. Göğüş et al. 2001;

A. J. van der Horst et al. 2012; L. Lin et al. 2013). Their X-ray spectra can generally be described equally well by models such as a double blackbody, optically thin thermal bremsstrahlung, or a Comptonized model (A. J. van der Horst et al. 2012). However, some bursts exhibit more thermal-like spectra that are adequately fitted only by a double blackbody or optically thin thermal bremsstrahlung model (G. L. Israel et al. 2008).

A more comprehensive multisource burst catalog was later compiled using data from Fermi/Gamma-ray Burst Monitor (GBM), which included bursts from more than eight magnetar sources, with the majority originating from 1E 1547.0−5408 (A. C. Collazzi et al. 2015). More recently, the INTErnational Gamma-Ray Astrophysics Laboratory (INTEGRAL)/Imager on Board the INTEGRAL Satellite (IBIS) combined over 20 yr of observations to construct a catalog of 1349 magnetar bursts (D. P. Pacholski et al. 2026). The timing and spectral properties reported in these catalogs are consistent with those obtained from earlier observations. In the 2020s, several magnetars underwent new outbursts that produced numerous short bursts. Detailed analyses have been conducted for bursts from Swift J1555.2−5402, SGR 1830−0645, and SGR 1935+2154 (T. Enoto et al. 2021; G. Younes et al. 2022; C.-P. Hu et al. 2025). While their general properties are similar to those of other magnetar bursts, the events from SGR 1935+2154 stand out with substantially longer durations, peaking around 1 s, which is significantly longer than other magnetars (G. Younes et al. 2020).

The longer-duration short bursts were observed during the 2020 outburst of SGR 1935+2154. During this outburst, a fast radio burst (FRB)-like event, FRB 200428, was detected and confirmed to be associated with a short burst from SGR 1935+2154 (C. D. Bochenek et al. 2020; CHIME/FRB Collaboration et al. 2020; S. Mereghetti et al. 2020). This discovery established SGR 1935+2154 as the only Galactic magnetar known to emit FRB-like bursts. Recently, another FRB-like event, FRB 221014A, from SGR 1935+2154 was also found to be associated with an X-ray burst from the same magnetar (C.-W. Wang et al. 2026). The FRB 200428-associated X-ray short burst has a similar duration to other short bursts from this source (C. K. Li et al. 2021), however, its spectrum is significantly softer (G. Younes et al. 2021). Beyond the distinctions seen within SGR 1935+2154 itself, L. Lin et al. (2013) reported systematic differences in duration distributions between magnetars. Together, these findings highlight the diversity of magnetar burst behavior, suggesting that physical conditions and emission mechanisms vary among sources and outbursts. A systematic comparison of bursts from multiple magnetars is therefore essential to constrain the physical origin and diversity of magnetar short bursts.

In this paper, we present a systematic study of magnetar short bursts using 8 yr of Neutron Star Interior Composition Explorer (NICER) observations. We compile a catalog of bursts from multiple magnetars, including the highly active SGR 1935+2154, as well as the magnetar-like pulsars, which are high-magnetic-field rotation-powered pulsars that exhibit magnetar-like bursts (F. P. Gavriil et al. 2008; R. F. Archibald et al. 2016; E. Göğüş et al. 2016). We perform a uniform timing and spectral analysis of these events and investigate correlations among their properties, as well as variations between different sources. This comprehensive analysis provides a uniform catalog of magnetar short bursts observed by NICER, offering a resource for future modeling and theoretical studies.

Table 1
NICER Observations Used for Each Magnetar and Magnetar-like Pulsar, along with the Total Number of Short Bursts Detected from Each Source

Magnetars	Number of Observations	Exposure (ks)	Number of Bursts
CXOU J010043.1−721134	241	725.0	4
4U 0142+61	166	330.0	4
SGR 0418+5729	16	21.3	0
SGR 0501+4516	198	498.9	0
1E 1048.1−5937	319	383.2	1
1E 1547.0−5408	60	87.9	0
Swift J1555.2−5402	68	118.1	74
PSR J1622−4950	22	46.0	0
CXOU J164710.2−455216	111	166.9	0
1RXS J170849.0−400910	113	84.9	1
CXOU J171405.7−381031	1	3.7	0
SGR J1745−2900	55	91.9	0
SGR 1806−20	15	37.2	4
XTE J1810−197	168	514.2	1
Swift J1818.0−1607	74	181.2	27
Swift J1822.3−1606	12	14.7	1
SGR 1830−0645	78	245.1	128
1E 1841−045	170	386.6	15
SGR 1900+14	1	0.4	0
SGR 1935+2154	415	1094.1	865
1E 2259+586	149	179.7	1
PSR J1119−6127[a]	111	157.0	0
PSR J1846−0258[a]	202	648.9	4
Total	2765	6016.9	1130

Note.
[a] Magnetar-like pulsars.

2. Data and Analysis

2.1. Data Selection and Reduction

NICER is a soft X-ray (0.2–12 keV) telescope mounted on the International Space Station (K. C. Gendreau et al. 2016). Its X-ray Timing Instrument (XTI) consists of 56 focal-plane modules (FPMs), though only 52 modules were in operation. While it does not offer imaging capability, NICER provides exceptionally high time resolution (∼300 ns) and a large effective area, making it ideal for studying transient events. For this work, we selected all NICER observations conducted from its launch, 2017 June, through 2025 June 30 that included a magnetar or a magnetar-like pulsar within the field of view. Among the 26 known magnetars (S. A. Olausen & V. M. Kaspi 2014),[17] NICER has observed 21 of them, along with two additional magnetar-like pulsars. We collected 6016.9 ks of exposure time from 2765 NICER observations across 23 sources. The total exposure time and number of observations used for each source are summarized in Table 1.

[17] McGill Online Magnetar Catalog: http://www.physics.mcgill.ca/~pulsar/magnetar/main.html.

Table 2
Details of NICER Observations on RXTE Blank-sky Regions after Excluding High-background Intervals

Sky Region	ObsID	Exposure (ks)	Counts
RXTE1	6012010106	3.1	1916
RXTE2	1012020169	18.6	6924
RXTE3	1012030123	5.3	2812
RXTE4	5012040217	8.3	4336
RXTE5	1012050131	5.8	4234
RXTE6	4012060255	13.3	7400
RXTE8	1012080190	12.2	5574

We used HEASOFT version 6.34 (Nasa High Energy Astrophysics Science Archive Research Center (HEASARC) 2014) to reduce the NICER data. The standard calibration and screening were performed by the task `nicerl2` with default options. The task `barycorr` was then applied with the JPLEPH.430 ephemeris to calibrate the time to Barycentric Dynamical Time (TDB). The resulting event lists were separated into the standard (0.5–8 keV) and high-energy (10–12 keV) bands for magnetar burst searches. On 2023 May 22, NICER sustained damage to its optical blocking film, leading to optical light leakage that degraded data quality. Observations taken after this date were processed separately. Nighttime data were reduced using the standard procedure described above. For daytime data, the `nicerl2` task was executed with a screening option of `threshfilter=DAY` to account for increased optical contamination.

2.2. Burst Search

We applied the Bayesian block algorithm implemented in the `astropy` package, using the `fitness=events` option, to both the standard and high-energy event lists to identify significant flux variations (J. D. Scargle 1998; J. D. Scargle et al. 2013). Blocks occurring during high-particle-background intervals, as defined by the high-energy band, were excluded. In the standard band, blocks with durations shorter than 1 s were selected as burst candidates. We further examined the FPM distribution of each candidate. Candidates with events concentrated in only one or two FPMs were identified as particle-induced events and excluded from the burst sample.

For each burst candidate, we estimated the statistical significance by computing the Poisson probability of detecting the observed number of counts within the burst block. A nearby interval of $\leqslant$5 s was selected to represent the nonburst count rate. After accounting for the number of trials, we retained only those blocks with a Poisson probability less than 10^{-5} for further analysis. The number of trials was defined as the total exposure time of each observation divided by 0.2 s, which is a typical magnetar burst duration (A. C. Collazzi et al. 2015).

NICER has been monitoring seven X-ray blank regions defined initially by the Rossi X-ray Timing Explorer (RXTE; K. Jahoda et al. 2006). We selected one observation from each region and excluded intervals with a high particle background. The details of the blank-sky observations used are summarized in Table 2. The RXTE7 region is excluded because it was later found to contain a faint X-ray source (R. A. Remillard et al. 2022). In addition, some of the remaining regions contain fainter sources (up to 3×10^{-13} erg s^{-1} cm^{-2}) according to the extended ROentgen Survey with an Imaging Telescope Array (eROSITA) source catalog (A. Merloni et al. 2024). We binned the cleaned event lists into 0.2 and 0.02 s bins, matching the burst durations reported in previous work (A. C. Collazzi et al. 2015) as well as those found in this study. We then recorded the total counts in each bin to characterize the background X-ray distribution. The cumulative distribution function reaches 100% at 4 counts per 0.2 s bin and 3 counts per 0.02 s bin (Figure 1). To ensure robust separation between genuine bursts and background fluctuations, we required that a burst candidate contain at least 5 counts within a Bayesian block. Based on the measured background rate and the NICER effective area, the expected detection limits for a transient event are approximately 2 and 2.5×10^{-11} erg cm^{-2} for transient durations of 0.02 and 0.2 s, respectively.

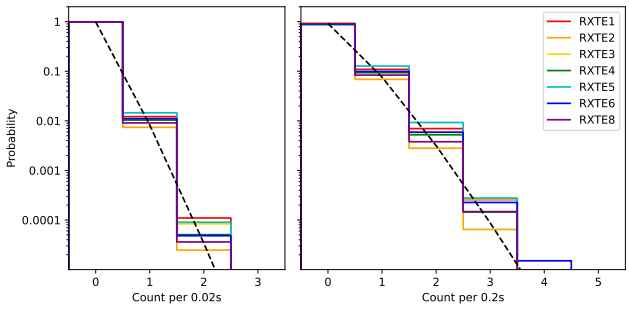

Figure 1. Distributions of background counts calculated with 0.02 s (left) and 0.2 s (right) time bins. Different colors correspond to the RXTE blank-sky regions identified in the legend. Black dashed lines are the Poisson probability mass function of averaged background counts calculated from Table 2.

2.3. Analysis

We first plotted the cumulative counts of each selected burst, after subtracting the nonburst count rate, and fitted the resulting curve with a step function (E. Göğüş et al. 2001). The step height corresponds to the total number of counts in the burst. This total count was then used to compute the 5% and 95% levels of the cumulative distribution. The time interval between when the cumulative count reaches 5% and 95% is defined as the T_{90} duration (C. Kouveliotou et al. 1993). For bursts with fewer than 20 total counts, the 5% fractional level corresponds to less than 1 count, making T_{90} not accurately defined. In these cases, T_{90} is instead defined as the duration of the corresponding Bayesian block.

The Bayesian blocks interval of each burst defines its good time interval (GTI), and the counts within this GTI were used for the spectral analysis. We first calculated the hardness ratio (HR), defined as

$$\mathrm{HR} = \frac{\mathrm{hard} - \mathrm{soft}}{\mathrm{hard} + \mathrm{soft}}, \quad (1)$$

where *soft* denotes photons in the 0.5–4 keV range and *hard* denotes photons in the 4–8 keV range. Some bursts show no photons below 2 keV because of strong absorption along the line of sight, so we adopted 4 keV as the boundary between the soft and hard photons, rather than the more typical 2 keV value.

We also extracted 0.5–8 keV burst spectra from the burst GTI with the task `nicerl3-spect` and performed spectral fitting using XSPEC v12.14 (HEASARC 2014). The nonburst interval used for estimating the burst significance was also adopted as the background spectrum for subtraction during fitting.

The spectra were binned according to the total number of burst counts: for bursts with fewer than 20 counts, at least 1 count per bin; for 20–49 counts, each bin contained at least 5 counts; for 50–249 counts, at least 10 counts per bin; and for more than 250 counts, at least 25 counts per bin. Each burst spectrum was fitted with both a blackbody and a power-law model. In all fits, the hydrogen column density ($N_{\rm H}$) was fixed to values reported in the literature for each of the magnetars (C.-P. Hu et al. 2020; A. Borghese et al. 2021; T. Enoto et al. 2021; G. Younes et al. 2022; C.-Y. Chu & H.-K. Chang 2023; C.-P. Hu et al. 2023). For bursts with fewer than 20 total counts, the blackbody temperature (kT) or the power-law photon index (Γ) was also fixed at 1.2 keV and 0.8, respectively. The `cstat` statistic in XSPEC was used for bursts with fewer than 250 counts, while the `chi` statistic was adopted for bursts with 250 counts or more. Once the best-fit parameters were obtained, we calculated the absorbed flux for both models in the 0.5–10 keV range. All uncertainties reported in this paper correspond to 1σ confidence levels.

3. Results and Discussion

3.1. Overall Samples

We detected a total of 1130 bursts in our dataset, including four from the magnetar-like pulsar PSR J1846−0258. The majority of events (76.5%) originated from SGR 1935+2154, which has been the most active magnetar in recent years. NICER captured its major outbursts in 2020 April, 2021 September, and 2022 October (G. Younes et al. 2020; T. Guver et al. 2021; C.-P. Hu et al. 2024, 2025), during which some FRB-like events were also contemporaneous (C. D. Bochenek et al. 2020; CHIME/FRB Collaboration et al. 2020; F. Kirsten et al. 2021; F. A. Dong & Chime/Frb Collaboration 2022; U. Giri et al. 2023).

Several magnetar outbursts have also been captured by NICER since its launch in 2017 June, including the 2020 outburst of Swift J1818.0−1607 (C.-P. Hu et al. 2020), the 2020 outburst of SGR 1830−0645 (G. Younes et al. 2022), the 2021 outburst of Swift J1555.2−5402 (T. Enoto et al. 2021), and the 2024 outburst of 1E 1841−045 (G. Younes et al. 2025). These sources accounted for 21.6% of the bursts in our sample. NICER also observed additional outbursts from other magnetars, such as XTE J1810−197 (T. Güver et al. 2019) and PSR J1846−0258 (C.-P. Hu et al. 2023). However, in these cases, the bursting activity was relatively weak and/or the observations did not coincide with the outburst onset, when the strongest bursting activity is typically observed.

The number of bursts detected from each source is summarized in Table 1, while details of individual bursts are provided in the Appendix. Several of these bursts have also been reported in earlier studies focused on individual sources, and here we place them in the broader context of the NICER magnetar sample.

3.2. T_{90} Duration

The distribution of T_{90} durations for all bursts is shown in Figure 2. The overall sample has a mean T_{90} of 350 ms and a standard deviation of 470 ms.

3.2.1. The Microsecond-scale Bursts

Two microsecond-scale bursts were identified in our sample: one from 1E 1048.1−5937 with a duration of 0.6 μs, and another from CXOU J010043.1−721134 with a duration of 5 μs. We note that CXOU J010043.1−721134 is located in the Small Magellanic Cloud (R. C. Lamb et al. 2002). We verified that these microsecond-scale bursts are not associated with known instrumental effects. The absolute timing precision of NICER (∼300 ns) is well below the measured burst durations. In each burst, the detected photons are distributed across multiple FPMs, with no single FPM registering more than one hit, which makes an instrumental or electronic origin unlikely.

To further examine whether such bursts are unique to magnetars, we applied the Bayesian block method to all available NICER RXTE blank-sky-region observations. Across a total exposure of 3308.9 ks, no microsecond-scale blocks were identified. Given an event rate of two per 6016.9 ks, the probability of observing zero events in 3308.9 ks is 33.3%. Although this probability is not sufficiently low to formally reject the null hypothesis, it provides additional support that the two detected microsecond-scale bursts are likely of astrophysical origin. We encourage future studies using NICER data to apply the Bayesian block method to search for similar microsecond-scale events.

These events represent the first detections of microsecond-scale X-ray bursts from magnetars. Their light curves are shown in Figure 3. Since no bursts were detected with durations between 10 μs and 1 ms, it remains unclear whether these events are simply the extreme tail of the main burst distribution or instead represent a distinct class of magnetar short bursts. One possible hint that microsecond-scale bursts differ from the main population is their extremely short duration, which may not allow sufficient time for the plasma to thermalize. Their emission is therefore expected to be nonthermal, in contrast to some normal bursts that can be described only by thermal models (G. L. Israel et al. 2008). Future X-ray missions with larger effective areas will be crucial to resolving this question.

3.2.2. Distinct T_{90} Distributions among Magnetars

Bursts from SGR 1935+2154 exhibit T_{90} values that are significantly longer than those of other magnetars. We fitted log-normal distributions to both groups and show the normalized distributions in the right panel of Figure 2. For SGR 1935+2154, the distribution peaks at 316 ms, while it peaks at 23 ms for the remaining magnetars. Thus, bursts from SGR 1935+2154 are on average about an order of magnitude longer. A Kolmogorov–Smirnov (KS) test applied to the two distributions yields a probability of 3.5×10^{-106}, confirming that the two samples are distinct. Nevertheless, a small subset of bursts from other magnetars extends to longer durations comparable to those of SGR 1935+2154, suggesting that long-duration bursts are not unique to this source and may be associated with source-dependent activity states.

G. Younes et al. (2020) studied bursts from SGR 1935+2154 during its 2020 outburst using NICER data. These events are also included in our sample, accounting for roughly 40% of the SGR 1935+2154 bursts analyzed here. However, the T_{90} durations we obtain are systematically shorter than those reported in G. Younes et al. (2020). A key reason is the different treatment of multipeak bursts: we apply a 0.2 s criterion to decide whether peaks belong to separate bursts, whereas their study used 0.5 s. Consequently, they grouped more peaks into single multipeak bursts, resulting in longer

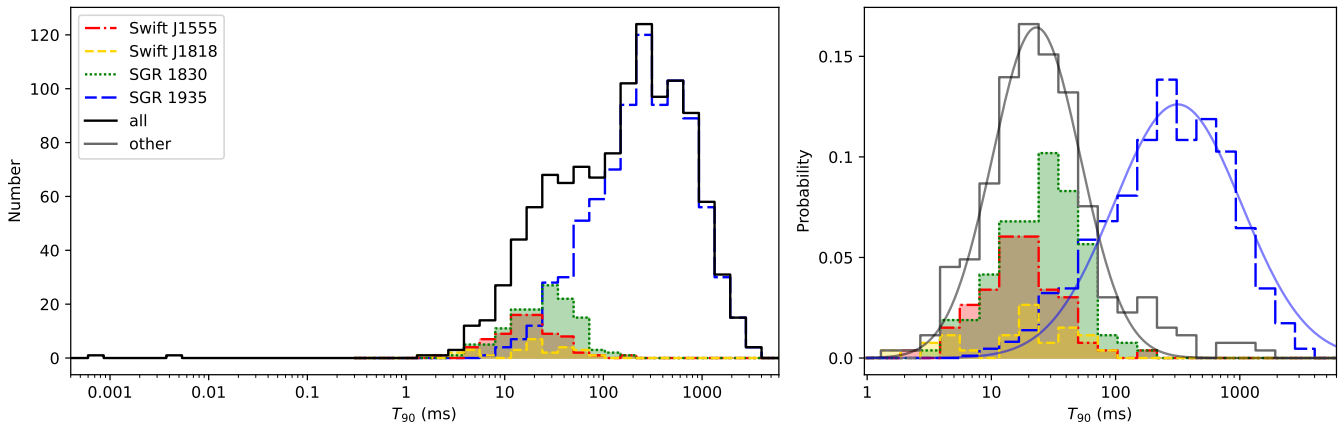

Figure 2. The left panel shows the overall duration distribution of the NICER magnetar bursts, and the right panel focuses on bursts with durations longer than 1 ms. In the right panel, the sample is divided into two groups: SGR 1935+2154 and all other magnetars, with each distribution normalized by its respective sample size so that their histogram sums to 1. The red dashed–dotted line represents Swift J1555.2−5402 (Swift J1555), the yellow dashed line represents Swift J1818.0−1607 (Swift J1818), and the green dotted line represents SGR 1830−0645 (SGR 1830). The histograms of these three samples are filled for clarity. The blue long-dashed line corresponds to SGR 1935+2154 (SGR 1935), and the black solid histogram represents all bursts. The gray histogram shows all samples except SGR 1935 +2154. The blue and the gray curves indicate the log-normal fits to the normalized SGR 1935+2154 and other samples, respectively.

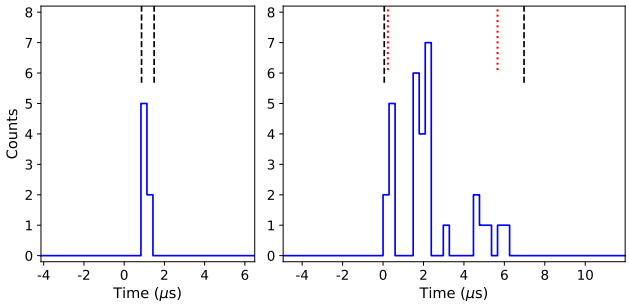

Figure 3. Light curves of the microsecond-scale bursts with 0.3 μs time bins. The left panel shows the burst with a T_{90} of 0.6 μs, with the zero-point at 2018-11-22T11:58:14.425441 (TDB). The right panel shows the burst with a T_{90} of 5 μs, with the zero-point at 2022-07-24T23:59:07.273212 (TDB). The black vertical dashed lines indicate the Bayesian block boundaries, and the red dotted lines mark the calculated T_{90} intervals.

measured T_{90} durations. A second factor is the difference in burst populations across epochs. NICER captured a burst storm from SGR 1935+2154 in the 2020 outburst, during which the persistent emission was higher than usual. Dim or very short bursts may have been buried in this elevated background and thus missed. In contrast, the bursts detected in the 2021 and 2022 outbursts occurred during lower persistent-emission states, making weaker and shorter events easier to identify. As a result, the 2021 and 2022 bursts exhibit shorter duration distributions overall, pulling the combined distribution toward smaller T_{90} values.

Regardless of methodology, the burst durations of SGR 1935+2154 differ significantly from those of other magnetars, suggesting possible intrinsic differences between this source and the broader magnetar population. SGR 1935 +2154 is currently the only Galactic magnetar known to produce FRB-like bursts (C. D. Bochenek et al. 2020; CHIME/FRB Collaboration et al. 2020), and numerous studies have explored what physical mechanisms might make it distinct. C.-P. Hu et al. (2025) reported that during the 2022 outburst of SGR 1935+2154, the burst properties evolved across different epochs, with a notable change after an intermediate flare. The X-ray bursts that occurred after the flare, including those around the time of the X-ray-associated FRB 221014A (F. A. Dong & Chime/Frb Collaboration 2022; C.-W. Wang et al. 2026), exhibit properties that differ significantly from the preflare burst population. G. Younes et al. (2021) also found that the X-ray counterpart of FRB 200428 exhibited a softer spectrum compared to typical bursts, potentially indicating an origin in a different region, more polar, of the magnetosphere. In this quasi-polar burst scenario, longer burst durations would be expected as field line foot points extend to larger altitudes.

These findings suggest that the differences in T_{90} durations between SGR 1935+2154 and other magnetars may reflect variations in the burst physics, geometry, and location across different outbursts and even between epochs within a single outburst. Our SGR 1935+2154 sample combines bursts from the 2020, 2021, and 2022 outbursts, and further disentangling these epoch-dependent effects will be necessary to understand the underlying physics. A detailed comparison of burst properties across different epochs of SGR 1935+2154 will be presented in a forthcoming paper (C.-Y. Chu et al. 2026, in preparation). Together, these results emphasize that SGR 1935+2154 is an exceptional case among magnetars, potentially connected to its unique ability to produce radio bursts.

In addition to bursts from other magnetars, L. Lin et al. (2013) reported 275 bursts from 1E 1547.0−5048 detected with Swift/X-ray Telescope (XRT), with a T_{90} distribution peaking at 207 ms and 262 bursts from SGR 0501+4516 detected with XMM-Newton, whose T_{90} durations peak at about 100 ms. A. C. Collazzi et al. (2015) presented a catalog of 440 bursts from at least eight magnetars observed by Fermi/GBM. Among these, 386 bursts originate from 1E 1547.0 −5048 and have a T_{90} peak at 156 ms, while the remaining bursts peak around 80 ms. Overall, these duration distributions are longer than those of the regular magnetar bursts in our NICER sample. One likely explanation is that NICER offers superior time resolution and larger effective area than those aforementioned missions: it is more sensitive to faint or shorter duration bursts. Consequently, our catalog includes a substantial number of short bursts, leading to systematically shorter T_{90} distributions compared to previous studies.

Table 3
Log-normal Fitting Results to T_{90} Duration Distributions from Different Magnetar Groups and Studies

Magnetars	Instrument	Peak (ms)	16%–84% Quantile (ms)
SGR 1935+2154	NICER/XTI	316	95–1026
Other magnetars	NICER/XTI	23	10–52
SGR 1935+2154[(1)]	NICER/XTI	840	430–1630
1E 1547.0−5408[(2)]	Swift/XRT	207	62–685
1E 1547.0−5408[(3)]	Fermi/GBM	156	62–389

References. (1) G. Younes et al. (2020). (2) L. Lin et al. (2013). (3) A. C. Collazzi et al. (2015).

Differences in energy coverage and background levels also play an important role. The Fermi/GBM catalog is based on observations in the 8–200 keV range, which differs significantly from the 0.5–8 keV band used in this work. In addition, Fermi/GBM has a higher background rate, which can cause the rising and decaying tails of bursts to be buried in the background. As a result, burst durations measured with GBM are often shorter than those measured with NICER, even for the same burst, as shown by G. Younes et al. (2021). This effect is also evident for 1E 1547.0−5048, where the T_{90} peak is longer in Swift/XRT data than in Fermi/GBM data, despite probing the same outburst (L. Lin et al. 2013; A. C. Collazzi et al. 2015). In contrast, most bursts from magnetars other than SGR 1935+2154 in our NICER catalog (e.g., Swift J1555.2−5402, Swift J1818.0−1607, and SGR 1830−0645) exhibit durations significantly shorter than those of 1E 1547.0−5048 detected by Fermi/GBM. This difference suggests that the bursts captured by GBM may be primarily sourced from more energetic bursting episodes, similar to the highly active 2020 outburst of SGR 1935+2154.

Interestingly, the 2009 outburst of 1E 1547.0−5048, from which the GBM bursts originate, was also accompanied by the detection of radio bursts (G. L. Israel et al. 2021). Although these radio bursts were less energetic than typical extragalactic FRBs and the FRB-like bursts associated with SGR 1935+2154, their occurrence may point to the existence of different magnetar outburst modes, some of which are characterized by more energetic X-ray bursting activity and an enhanced likelihood of radio burst emission. In contrast, searches for radio burst events from several other magnetars have been conducted but yielded no detections (A. Geminardi et al. 2025).

A summary of the log-normal fitting results of the T_{90} distributions, including the peak values and 16%–84% quantile ranges for different groups and instruments, is presented in Table 3.

3.3. Hardness Ratio

The distribution of the HR is shown in Figure 4. The overall distribution has a mean of −0.29 and a standard deviation of 0.31. Most bursts exhibit relatively soft spectra, while those from Swift J1555.2−5402 and Swift J1818.0−1607 are noticeably harder, with an HR mostly greater than zero. This trend is consistent with the higher column densities of these sources ($N_{\rm H}$ = 8.72 and 11.2 × 10^{22} atoms cm^{-2}, respectively), which preferentially absorb more soft photons compared to other magnetars.

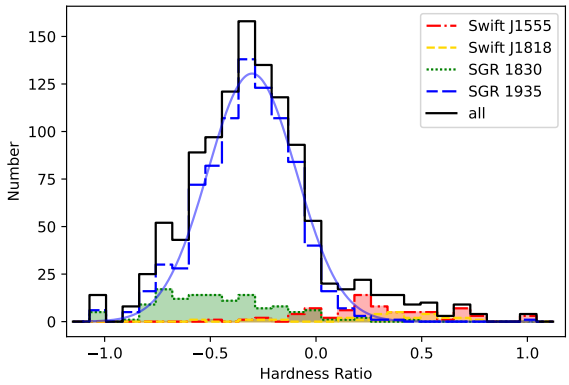

Figure 4. Hardness ratio distribution of all bursts. Different histograms represent magnetar groups as defined in Figure 2 and indicated in the legend. The blue curve shows the normal distribution fit to the SGR 1935+2154 sample.

For SGR 1935+2154, the HR distribution is well described by a normal distribution with a mean of −0.30 and a standard deviation of 0.21. This distribution is similar to those of other low-$N_{\rm H}$ magnetars, in contrast to the marked differences observed in their burst-duration distributions.

3.4. Spectral Model

The spectra of magnetar bursts in the soft X-ray band can be equally well described by either a single power-law or a single blackbody model (e.g., D. Kırmizibayrak et al. 2017). Therefore, each burst spectrum was fitted individually with both models to account for both possibilities.

3.4.1. Flux

The results of the power-law spectral fits are shown in Figure 5, which display the distributions of photon index (Γ) and corresponding flux ($F_{\rm PL}$). A normal distribution fit to the SGR 1935+2154 group yields a mean Γ of 0.45 and a standard deviation of 0.44. The photon index is slightly softer than that of Fermi/GBM bursts (∼0; A. C. Collazzi et al. 2015). The difference likely reflects NICER's higher sensitivity to fainter bursts, which tend to exhibit softer spectra (E. Göğüş et al. 2001; L. Lin et al. 2013), corresponding to a larger photon index (see also Section 3.5). As a result, the inclusion of additional dim bursts shifts the overall Γ distribution toward higher values.

The results of the blackbody fits are shown in Figure 6, which presents the distributions of blackbody temperature (kT) and flux ($F_{\rm BB}$). Fitting the kT distribution of the SGR 1935+2154 group with a log-normal function yields a peak at 1.56 keV and a 16%–84% quantile range of 1.17–2.08 keV. This characteristic temperature is slightly lower than that obtained from Swift/XRT bursts of 1E 1547.0−5408 (∼2.5 keV; L. Lin et al. 2013) and considerably lower than that of Fermi/GBM bursts (∼4.5 keV; A. C. Collazzi et al. 2015). Similar selection effects likely explain the lower characteristic temperature compared to Swift/XRT and Fermi/GBM results. Because NICER is more sensitive to faint, softer bursts, the inclusion of these events shifts the overall kT distribution toward lower values. The higher temperatures inferred from Fermi/GBM may also arise because those fits correspond to the lower-temperature component of a two-blackbody model in the 8–200 keV range, where the cooler component is poorly constrained and thus

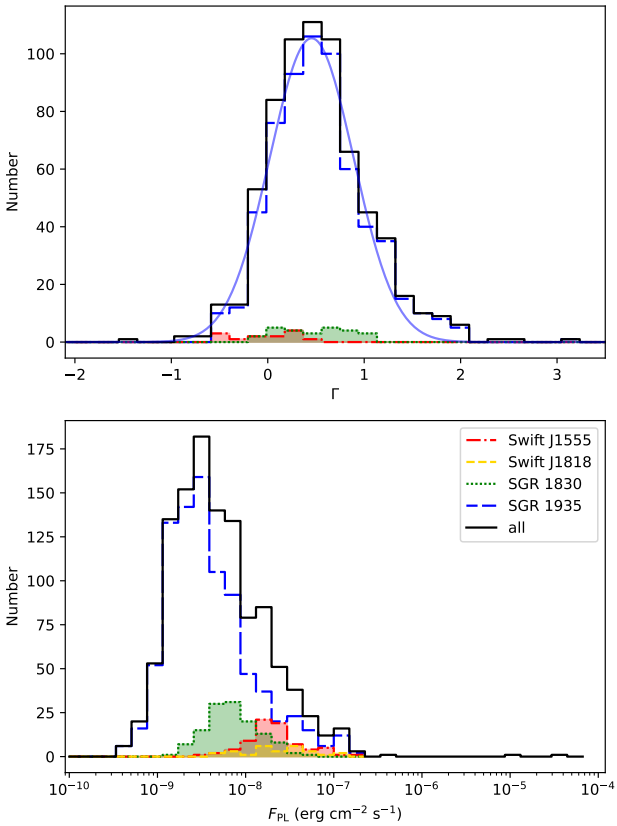

Figure 5. Photon index Γ (top) and flux F_{PL} (bottom) distributions of all bursts. Different histograms represent magnetar groups as defined in Figure 2 and indicated in the legend. For the Γ distribution, most Swift J1818.0−1607 bursts have fixed Γ values during spectral fitting; therefore, this sample is not plotted separately on the top panel.

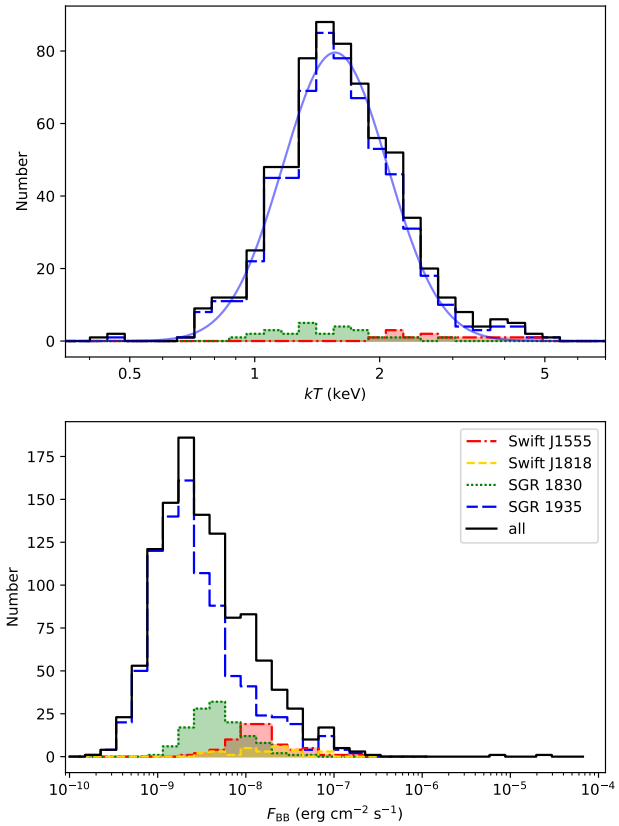

Figure 6. Blackbody temperature kT (top) and flux F_{BB} (bottom) distributions of all bursts. Different histograms represent magnetar groups as defined in Figure 2 and indicated in the legend. For the kT distribution, most Swift J1818.0−1607 bursts have fewer than 20 counts, and their kT values were fixed during spectral fitting; therefore, this sample is not plotted separately on the top panel.

biased upward. Alternatively, the broadband spectra may be better represented by three blackbody components rather than two. In any case, the burst temperatures are significantly higher than the typical magnetar temperature in quiescence of ∼0.45 keV (C.-Y. Chu & H.-K. Chang 2023), and even during the onset of outburst of ∼1.2 keV (e.g., C.-P. Hu et al. 2020; T. Enoto et al. 2021). The fluxes are generally distributed between 10^{-10} and 3×10^{-7} erg s^{-1} cm^{-2}, with the two microsecond-scale bursts showing much higher fluxes of $\sim 10^{-5}$ erg s^{-1} cm^{-2}.

The flux distribution obtained from the power-law model is broadly consistent with that derived from the blackbody model, indicating that the inferred burst fluxes are not strongly dependent on the chosen spectral model.

We also calculate the emission radius (R) from the normalization of the blackbody flux. The distribution of R is shown in the top panel of Figure 7. The distances used to calculate R are adopted from S. A. Olausen & V. M. Kaspi (2014), C.-Y. Chu & H.-K. Chang (2023), and the references therein, as well as T. Enoto et al. (2021) and G. Younes et al. (2022). Fitting the R distribution of the SGR 1935+2154 group with a log-normal function yields a peak at 5.0 km and a 16%–84% quantile range of 3.4–7.4 km. The size of the thermal emitting region is mostly consistent with previous work (G. Younes et al. 2020). Most bursts show R values larger than the typical emitting size of surface thermal emission from neutron stars, about 3 km (e.g., H.-K. Chang et al. 2023; C.-Y. Chu & H.-K. Chang 2023). This suggests that the burst emission likely originates from a fireball at higher altitude rather than directly from the neutron star surface.

The R distribution of Swift J1555.2−5402 has a mean of 22 km when calculated assuming a distance of 10 kpc at the Scutum–Centaurus Arm (T. Enoto et al. 2021), which is significantly larger than that of other magnetars. We consider that this discrepancy mainly arises from the distance estimate. The placement of Swift J1555.2−5402 at the Scutum–Centaurus Arm was motivated by the fact that another magnetar in the same direction, 1E 1547.0−5408, is estimated to lie at 4.5 kpc near the Perseus Arm (A. Tiengo et al. 2010). Since Swift J1555.2−5402 has an N_H value roughly twice that of 1E 1547.0−5408, it was suggested to reside in a more distant spiral arm (T. Enoto et al. 2021). If Swift J1555.2−5402 is instead placed at a distance of 4.5 kpc, the inferred emission radius becomes more consistent with those of other magnetars. This suggests that Swift J1555.2−5402 may lie at a similar distance to 1E 1547.0−5408 but in a denser local environment. Even with this assumption, the R distribution of Swift J1555.2−5402, with a mean of about 10 km, remains somewhat larger than that of other magnetars, possibly indicating a different emission geometry that produces a larger fireball area. The R distribution assuming a distance of 10 kpc is shown as the unshaded red histogram in Figure 7, while the distribution for 4.5 kpc is shown as the shaded red histogram. The R values of Swift J1555.2−5402 reported in the Table A1 are calculated assuming a distance of 4.5 kpc.

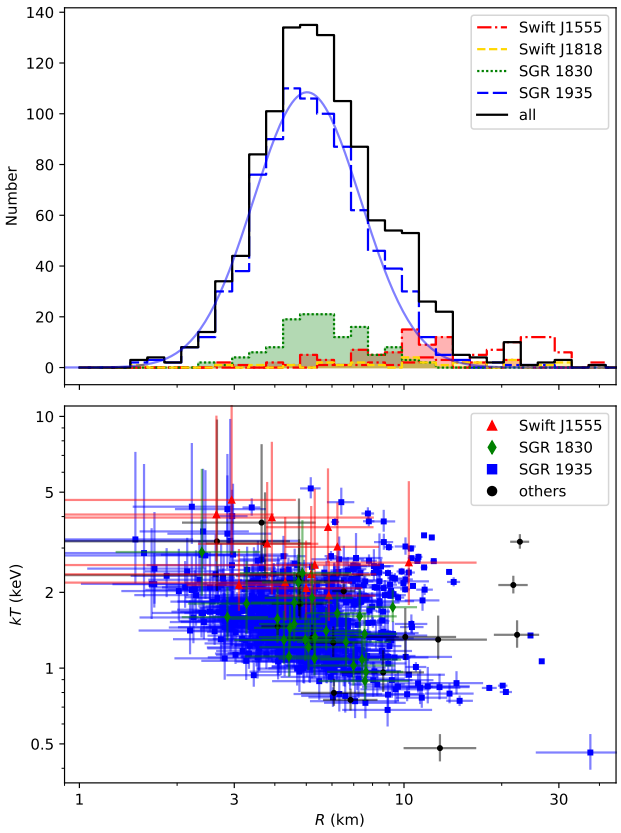

Figure 7. Distribution of blackbody emission radius R (top) and emission radius R versus temperature kT (bottom). Different histograms represent the magnetar groups defined in Figure 2, as indicated in the legend. The unshaded red histogram shows Swift J1555.2−5402 assuming a distance of 10 kpc, while the shaded red histogram assumes a distance of 4.5 kpc. The blue curve shows the log-normal fit to the R distribution of the SGR 1935+2154 sample. In the bottom panel, red triangles represent Swift J1555.2−5402, green diamonds represent SGR 1830−0645, blue squares represent SGR 1935 +2154, and black circles represent the remaining magnetars.

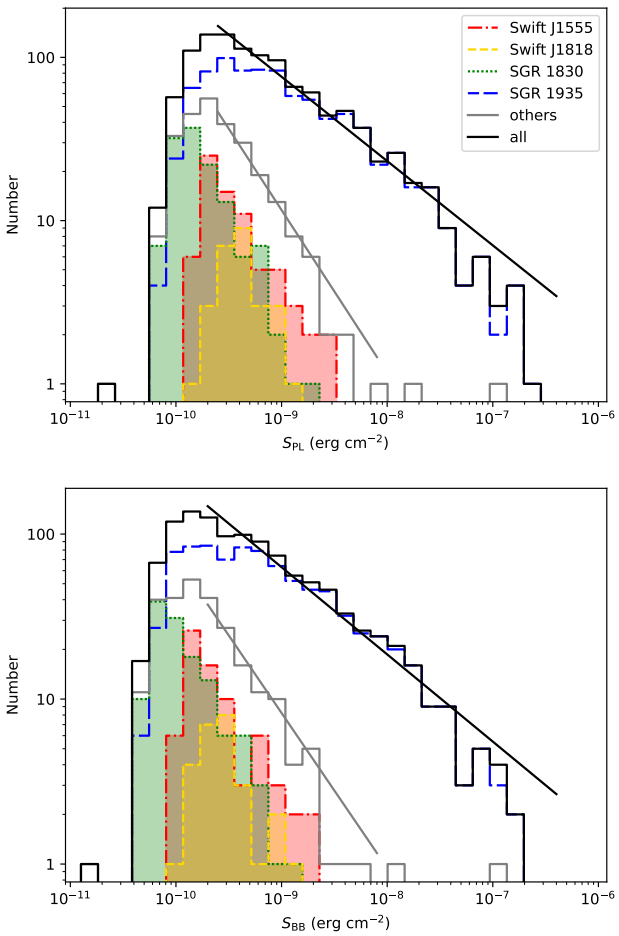

Figure 8. Fluence distributions derived from the power-law model S_{PL} (top) and the blackbody model S_{BB} (bottom) for all bursts. Different histograms represent magnetar groups as defined in Figure 2 and indicated in the legend. The black lines show the best-fit power-law functions for the full burst sample, with indices of -0.52 ± 0.03 for the power-law model and -0.53 ± 0.04 for the blackbody model. The gray lines show the best-fit power-law functions for the sample excluding SGR 1935+2154, with indices of -1.00 ± 0.06 and -0.94 ± 0.06 for the two spectral models.

The bottom panel of Figure 7 shows the relation between R and kT. An overall anticorrelation is observed, as expected for blackbody emission. We note that the microsecond-scale bursts are not included in this figure because their inferred emission radii are unphysically large (1000 and 36,000 km), which further supports a nonthermal origin for these events.

3.4.2. Fluence

The fluence (S_{PL} and S_{BB}) distributions, calculated from the fluxes and T_{90} durations, for both the power-law and blackbody models are shown in Figure 8 as log(S)–log(N) plots. For fluences above 2×10^{-10} erg cm^{-2}, the distributions are well described by power laws, yielding indices of -0.52 ± 0.03 for the power-law model and -0.53 ± 0.04 for the blackbody model. Because the full sample is dominated by SGR 1935+2154, we also fit the distributions after excluding its bursts. This yields significantly steeper slopes of -1.00 ± 0.06 for the power-law model and -0.94 ± 0.06 for the blackbody. These results demonstrate that SGR 1935+2154 exhibits a distinct fluence distribution compared to other magnetars. Its longer burst durations lead to a larger number of high-fluence events, which strongly influences the overall distribution. This further supports the idea that SGR 1935+2154 underwent a different outburst mode during its active episodes in 2020–2022 compared with other magnetars.

From the turnover in these distributions, we estimate that NICER achieves nearly 100% detection efficiency above 2×10^{-10} erg cm^{-2}, with a detection limit of approximately 4×10^{-11} erg cm^{-2}. For the duration distribution of our burst sample, this detection limit is slightly higher than the expected value of 2.5×10^{-11} erg cm^{-2} estimated in Section 2.2. The reason is that most of the bursts identified in this work occurred during a magnetar X-ray outburst, where the persistent emission is higher. As a result, the background level is higher, and some low-fluence bursts are buried in the background.

3.5. Correlation

3.5.1. Spectral versus Spectral

The left panels of Figure 9 show the distributions of Γ and kT versus their corresponding fluxes. For low-count bursts, where Γ or kT were fixed during fitting, these events are excluded from the figure and from the correlation analysis. Overall, bursts with higher fluxes tend to exhibit harder spectra, characterized by higher temperatures or smaller photon indices, consistent with previous studies (see, e.g., E. Göğüş et al. 2001; L. Lin et al. 2013). To quantify this relation, we calculated Pearson correlation coefficients (Pearson r) for bursts from SGR 1935

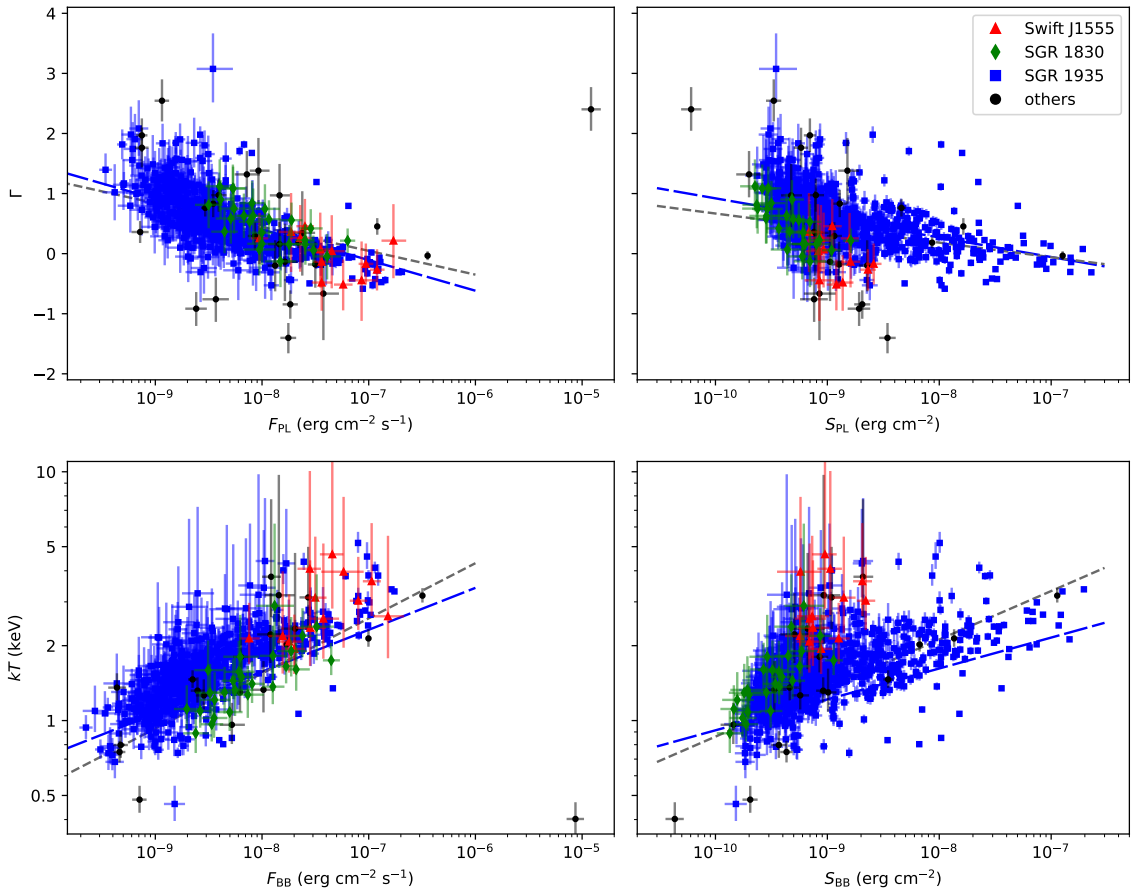

Figure 9. Distribution of spectral parameters. Different data points represent magnetar groups as defined in Figure 7 and indicated in the legend. The blue long-dashed lines and the gray dashed lines show the best-fit power-law relations for SGR 1935+2154 and for all other magnetars, respectively.

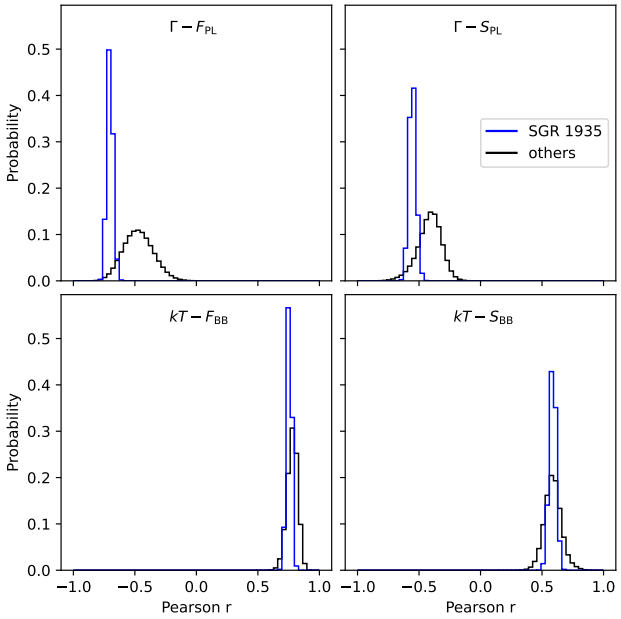

Figure 10. Distributions of Pearson correlation coefficients between spectral parameters obtained using the bootstrap method. The parameter combinations are indicated at the top of each panel. The blue and the black histograms represent the SGR 1935+2154 sample and all other magnetar samples, respectively.

+2154 and from other magnetars separately. The clear outlier, the 5 μs burst from CXOU J010043.1−721134, was excluded from this analysis.

For SGR 1935+2154, the coefficients are −0.702 for Γ versus F_{PL} and 0.754 for kT versus F_{BB}. For the other magnetar bursts, the corresponding values are −0.556 and 0.807, respectively. Strong correlations are found in all cases, except for the weaker Γ–F_{PL} relation in the other magnetar sample. We fitted power-law functions to these highly correlated relations, obtaining indices of -0.51 ± 0.03 and -0.42 ± 0.08 for SGR 1935+2154 and the other magnetars, respectively, for the Γ–F_{PL} relation. For the kT–F_{BB} relation, the indices are 0.18 ± 0.01 for SGR 1935+2154 and 0.22 ± 0.02 for the remaining magnetars. In addition to the microsecond burst, two other events exhibit notably soft spectra ($kT < 0.5$ keV or $\Gamma > 2.5$): one from SGR 1935+2154 and one from 4U 0142+61.

The right panels of Figure 9 show the distributions of Γ and kT versus S_{PL} and S_{BB}, respectively. Similar to the flux relations, bursts with higher fluences generally exhibit harder spectra. For SGR 1935+2154, the Pearson correlation coefficients are −0.554 for Γ versus S_{PL} and 0.588 for kT versus S_{BB}, while for the other magnetar bursts, they are −0.411 and 0.574, respectively. The correlations weaken when moving from flux to fluence, as the scatter increases at higher fluences, suggesting the presence of possible subgroups. However, after incorporating the duration parameter, the 5 μs burst aligns with the overall trend, remaining consistent with the main burst population.

We also examined the fluence relations using power-law fits. For the Γ–S_{PL} relation, the derived indices are -0.32 ± 0.03 for SGR 1935+2154 and -0.28 ± 0.07 for the other

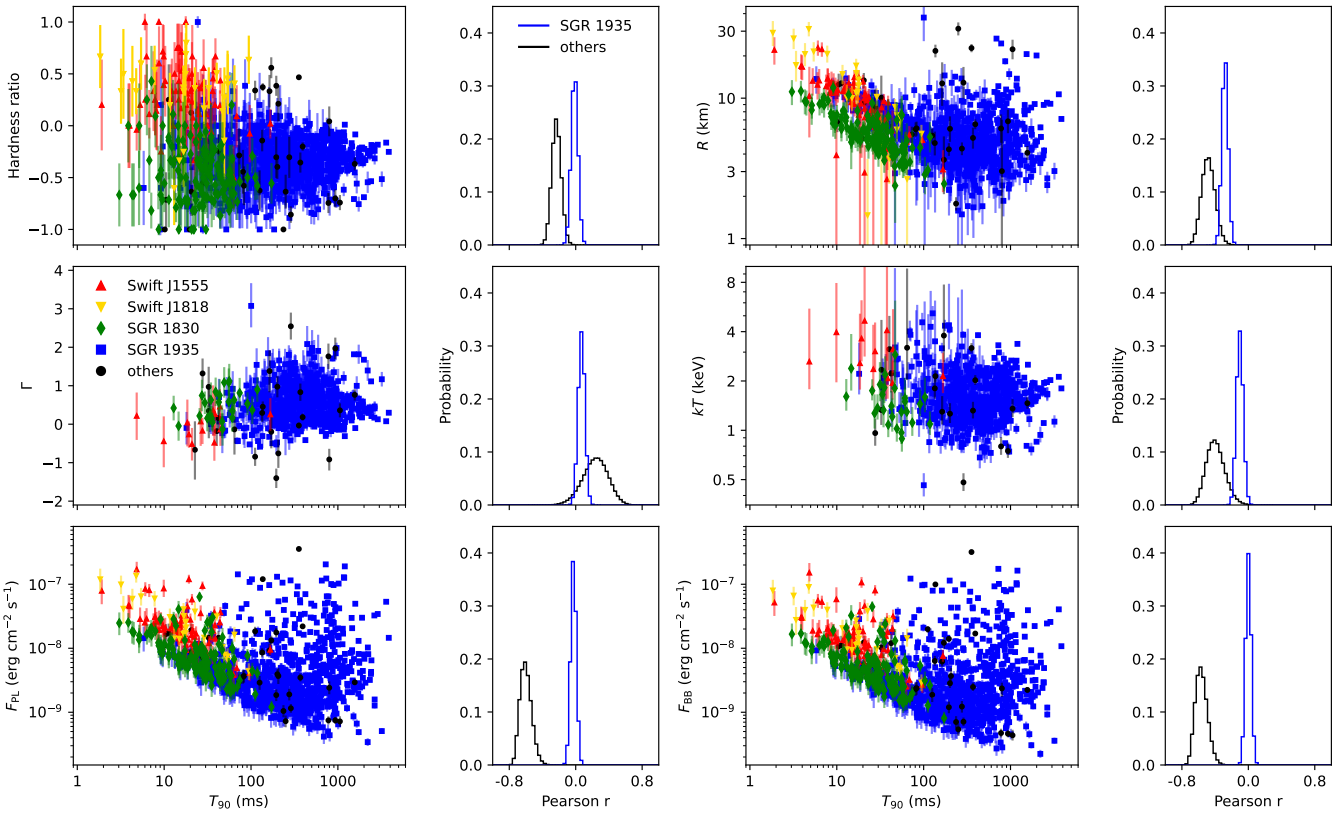

Figure 11. Distributions of T_{90} versus spectral parameters for all bursts (scatter plots) and the corresponding distributions of Pearson correlation coefficients obtained from bootstrap resampling (histograms). Data points in the scatter plots represent magnetar groups as defined in Figure 9, with the yellow triangles indicating Swift J1818.0−1607. The blue and the black histograms correspond to the SGR 1935+2154 sample and all other magnetars, respectively. The two microsecond-scale bursts are excluded from this correlation analysis.

magnetars. In the kT–S_{BB} relation, the indices are 0.13 ± 0.01 for SGR 1935+2154 and 0.19 ± 0.02 for the remaining sources. Because these fits are driven primarily by the high-fluence end of the distribution, the results appear weaker and less well defined than those seen in the flux relations.

To further investigate possible subgroups within our sample, we performed a bootstrap analysis of the spectral correlations. For each selected burst sample, we generated a resampled dataset by randomly selecting bursts from the original sample until the resampled dataset matched the original in size. Each burst could be selected multiple times. We then recalculated the Pearson correlation coefficient for each resampled dataset. This process was repeated 1 million times, and the resulting distributions of correlation coefficients are shown in Figure 10.

The mean correlation coefficients derived from the bootstrap analysis are consistent with those obtained from the original samples across all parameter combinations. However, the coefficient distributions for the other magnetar bursts are noticeably broader than those for the SGR 1935+2154 sample, particularly for the power-law model. This wider spread likely reflects the inclusion of bursts from multiple magnetars, whose spectral parameters may be influenced by instrumental limitations and varying absorption along different lines of sight. The bootstrap results show no additional outlying behavior, and no secondary clusters or anomalous distributions appear across the 1 million trials. This suggests that all bursts follow a similar trend, except for the 5 μs burst in the flux relation.

3.5.2. Timing versus Spectral

The correlations between burst duration and spectral parameters are shown in Figure 11, along with their bootstrap distributions. As with the spectral–spectral relations, bursts were divided into two groups: SGR 1935+2154 and all other magnetars. The two microsecond-scale bursts were excluded from the analysis. For SGR 1935+2154, all correlations between T_{90} and the spectral parameters are statistically insignificant, with Pearson coefficients consistent with zero. This is consistent with earlier studies of magnetar bursts, which also found no clear correlation between timing and spectral properties (A. J. van der Horst et al. 2012).

In contrast, for the other magnetars, both F_{PL} and F_{BB} show an apparent anticorrelation with T_{90}. This trend is not intrinsic but instead results from instrumental limitations. Bursts with lower fluence are more likely to fall below the detection threshold, truncating the intrinsic burst population. The observed anticorrelation is therefore a selection effect. Similarly, the weak correlations and anticorrelations between T_{90} and HR, R, kT, and Γ, can be explained by the same detection bias. Shorter bursts tend to have lower fluxes, and as shown in Figure 10, fainter bursts generally display softer spectra. This leads to the weak correlations between duration and spectral parameters observed here.

4. Summary

In this study, we constructed a comprehensive catalog of magnetar short bursts spanning 8 yr of NICER observations.

We identified a total of 1130 bursts and most of these bursts originated from SGR 1935+2154, which contributed 865 events. We present the distributions of timing and spectral parameters for all detected bursts and investigate their correlations. The bursts from SGR 1935+2154 generally show longer T_{90} durations than those from other magnetars. We also report the first detection of microsecond-scale bursts in magnetars, one from 1E 1048.1−5937 and another from CXOU J010043.1−721134.

Bursts with higher fluxes tend to exhibit harder spectra, indicating higher blackbody temperatures in the blackbody model or lower photon indices in the power-law model. The bootstrap resampling analysis confirms that these spectral correlations are statistically robust, while correlations between burst duration and spectral parameters remain weak or absent. The weaker correlations found among other magnetars likely reflect differences in source properties and instrumental effects.

This catalog provides a uniform, statistically rich sample that will serve as a foundation for future investigations of magnetar burst energetics, emission mechanisms, and magnetic field dynamics.

Acknowledgments

This research has made use of data and software provided by the High Energy Astrophysics Science Archive Research Center (HEASARC), which is a service of the Astrophysics Science Division at NASA/GSFC. C.-Y.C. acknowledges support from the National Science and Technology Council (NSTC) in Taiwan through grants 113-2811-M-018-003-MY2 and 112-2112-M-018-004-MY3. C.-P.H. acknowledges support from the NSTC in Taiwan through grant 112-2112-M-018-004-MY3. S.G. acknowledges the support of the CNES. W.C.G.H. acknowledges support through grant 80NSSC23K0078 from NASA. M.L.B. acknowledges support from the Max Planck Society.

Facility: NICER.

Software: Heasoft (HEASARC 2014).

Appendix
The Catalog

This appendix presents example bursts identified in this study. A complete burst catalog can be found in the online version of Table A1.

Table A1
Magnetar Burst Catalog

Magnetar	Burst	ObsID	TDB Start	T_{90} (ms)	HR	kT [a] (keV)	R [a] (km)	log$F_{\rm BB}$ (erg cm^{-2} s^{-1})	Γ	log$F_{\rm PL}$ (erg cm^{-2} s^{-1})
CXOU J010043.1−721134	1	5505010502	2022-07-24T23:59:07.273	0.005	-0.87 ± 0.09	$0.40^{+0.07}_{-0.05}$	36,000[b]	$-5.06^{+0.08}_{-0.08}$	$2.40^{+0.37}_{-0.36}$	$-4.92^{+0.09}_{-0.09}$
	4	5505011704	2023-07-31T20:21:10.490	1055.592	-0.74 ± 0.07	$1.36^{+0.19}_{-0.15}$	$22.3^{+3.8}_{-3.4}$	$-9.36^{+0.09}_{-0.08}$	$0.36^{+0.18}_{-0.18}$	$-9.14^{+0.08}_{-0.08}$
4U 0142+61	1	0020040102	2017-07-15T14:15:37.947	27.684	-0.56 ± 0.16	$0.96^{+0.22}_{-0.16}$	$8.6^{+2.9}_{-2.3}$	$-8.28^{+0.12}_{-0.11}$	$1.32^{+0.39}_{-0.38}$	$-8.14^{+0.12}_{-0.11}$
	4	6020040102	2023-09-26T11:56:38.889	287.419	-0.86 ± 0.08	$0.48^{+0.07}_{-0.06}$	$12.9^{+3.8}_{-2.9}$	$-9.15^{+0.07}_{-0.07}$	$2.54^{+0.36}_{-0.34}$	$-8.94^{+0.07}_{-0.07}$
1E 1048.1−5937	1	1020240141	2018-11-22T11:58:14.425	0.001	-0.71 ± 0.26	1.20	1000[b]	$-4.55^{+0.15}_{-0.17}$	0.80	$-4.38^{+0.15}_{-0.17}$
Swift J1555.2−5402	1	4202190101	2021-06-03T13:58:12.407	15.382	-0.27 ± 0.29	1.20	$11.5^{+1.8}_{-1.7}$	$-7.85^{+0.12}_{-0.14}$	0.80	$-7.67^{+0.12}_{-0.14}$
	74	4560013017	2021-10-23T06:18:22.667	22.435	-0.33 ± 0.31	1.20	$9.6^{+1.6}_{-1.6}$	$-8.00^{+0.14}_{-0.15}$	0.80	$-7.82^{+0.14}_{-0.15}$
1RXS J170849.0−400910	1	3622050401	2020-04-03T18:13:10.886	111.437	0.34 ± 0.09	⋯	⋯	$-7.70^{+0.04}_{-0.06}$	$-0.84^{+0.23}_{-0.24}$	$-7.74^{+0.07}_{-0.07}$
SGR 1806−20	1	5020410102	2023-02-25T00:23:44.944	136.532	0.37 ± 0.04	$2.14^{+0.19}_{-0.16}$	$21.7^{+2.3}_{-2.2}$	$-7.00^{+0.03}_{-0.02}$	$0.45^{+0.14}_{-0.14}$	$-6.92^{+0.02}_{-0.02}$
	4	5020410103	2023-02-28T21:10:53.593	355.533	0.47 ± 0.02	$3.18^{+0.23}_{-0.20}$	$22.8^{+1.6}_{-1.5}$	$-6.50^{+0.01}_{-0.01}$	$-0.03^{+0.07}_{-0.07}$	$-6.45^{+0.01}_{-0.01}$
XTE J1810−197	1	2020420105	2019-03-31T22:57:55.917	195.301	0.38 ± 0.10	⋯	⋯	$-7.85^{+0.04}_{-0.05}$	$-1.40^{+0.25}_{-0.26}$	$-7.75^{+0.07}_{-0.08}$
Swift J1818.0−1607	1	3201060101	2020-03-13T04:47:22.249	17.981	0.80 ± 0.19	1.20	$12.3^{+2.0}_{-1.9}$	$-7.85^{+0.13}_{-0.14}$	0.80	$-7.67^{+0.13}_{-0.14}$
	27	3556015201	2020-08-25T09:48:03.712	53.695	0.46 ± 0.27	1.20	$7.3^{+1.1}_{-1.1}$	$-8.30^{+0.12}_{-0.14}$	0.80	$-8.13^{+0.12}_{-0.14}$
Swift J1822.3−1606	1	1020460110	2018-04-11T19:53:02.682	206.345	0.21 ± 0.17	⋯	⋯	$-8.43^{+0.13}_{-0.16}$	$-0.76^{+0.36}_{-0.38}$	$-8.43^{+0.12}_{-0.13}$
SGR 1830−0645	1	3201810102	2020-10-11T13:13:22.627	14.583	-0.14 ± 0.37	1.20	$5.3^{+1.0}_{-1.0}$	$-8.42^{+0.15}_{-0.17}$	0.80	$-8.25^{+0.15}_{-0.17}$
	128	4201810109	2021-03-22T05:28:50.886	28.740	-0.27 ± 0.29	1.20	$4.9^{+0.8}_{-0.7}$	$-8.49^{+0.12}_{-0.14}$	0.80	$-8.32^{+0.12}_{-0.14}$
1E 1841−045	1	7020500115	2024-08-21T05:47:16.995	275.708	-0.30 ± 0.20	1.20	$4.4^{+0.5}_{-0.5}$	$-8.91^{+0.09}_{-0.09}$	0.80	$-8.72^{+0.09}_{-0.09}$
	15	7582010112	2024-11-09T19:06:31.623	82.960	-0.58 ± 0.19	1.20	$6.1^{+0.7}_{-0.7}$	$-8.62^{+0.10}_{-0.10}$	0.80	$-8.43^{+0.10}_{-0.10}$
SGR 1935+2154	1	3020560101	2020-04-28T00:42:04.992	200.675	-0.17 ± 0.15	$2.09^{+0.80}_{-0.44}$	$2.5^{+0.8}_{-0.7}$	$-8.66^{+0.12}_{-0.12}$	$0.21^{+0.34}_{-0.35}$	$-8.57^{+0.10}_{-0.10}$
	867	5576010116	2022-11-15T11:48:59.834	222.401	-0.37 ± 0.21	1.20	$4.7^{+0.6}_{-0.5}$	$-8.97^{+0.10}_{-0.10}$	0.80	$-8.78^{+0.10}_{-0.10}$

Table A1
(Continued)

Magnetar	Burst	ObsID	TDB Start	T_{90} (ms)	HR	kT [a] (keV)	R [a] (km)	$\log F_{\rm BB}$ (erg cm^{-2} s^{-1})	Γ	$\log F_{\rm PL}$ (erg cm^{-2} s^{-1})
1E 2259+586	1	7020600108	2024-12-27T21:14:02.224	236.260	-1.00 ± 0.00	1.20	$1.8^{+0.2}_{-0.2}$	$-9.15^{+0.09}_{-0.10}$	0.80	$-8.98^{+0.09}_{-0.10}$
PSR J1846−0258	1	3033290103	2020-08-05T17:08:55.807	20.480	0.12 ± 0.25	1.20	$13.4^{+1.7}_{-1.6}$	$-7.91^{+0.10}_{-0.11}$	0.80	$-7.72^{+0.10}_{-0.11}$
	4	3598010801	2020-07-25T19:38:03.338	11.285	0.25 ± 0.34	1.20	$12.8^{+2.3}_{-2.2}$	$-7.95^{+0.14}_{-0.16}$	0.80	$-7.76^{+0.14}_{-0.16}$

Notes.
[a] Values of kT or R that could not be constrained during spectral fitting are marked with "…."
[b] Uncertainties are not shown here for clarity but are provided in the full catalog table.

(This table is available in its entirety in machine-readable form in the online article.)

ORCID iDs

Che-Yen Chu https://orcid.org/0009-0002-2845-2343
Chin-Ping Hu https://orcid.org/0000-0001-8551-2002
Teruaki Enoto https://orcid.org/0000-0003-1244-3100
George A. Younes https://orcid.org/0000-0002-7991-028X
Rachael Stewart https://orcid.org/0000-0002-0254-5915
Zaven Arzoumanian https://orcid.org/0009-0008-6187-8753
Wynn C. G. Ho https://orcid.org/0000-0002-6089-6836
Zorawar Wadiasingh https://orcid.org/0000-0002-9249-0515
Andrea Sanna https://orcid.org/0000-0002-0118-2649
Sebastien Guillot https://orcid.org/0000-0002-6449-106X
Gaurava K. Jaisawal https://orcid.org/0000-0002-6789-2723
Matthew G. Baring https://orcid.org/0000-0003-4433-1365
Marlon L. Bause https://orcid.org/0009-0006-3567-981X
Tolga Güver https://orcid.org/0000-0002-3531-9842
Chryssa Kouveliotou https://orcid.org/0000-0003-1443-593X
Alex Van Kooten https://orcid.org/0000-0002-3905-4853
Keith C. Gendreau https://orcid.org/0000-0001-7115-2819

References

Archibald, R. F., Kaspi, V. M., Tendulkar, S. P., & Scholz, P. 2016, ApJL, 829, L21
Bochenek, C. D., Ravi, V., Belov, K. V., et al. 2020, Natur, 587, 59
Borghese, A., Rea, N., Turolla, R., et al. 2021, MNRAS, 504, 5244
Chang, H.-K., Hsiang, J.-Y., Chu, C.-Y., et al. 2023, MNRAS, 520, 4068
CHIME/FRB Collaboration, Andersen, B. C., Bandura, K. M., et al. 2020, Natur, 587, 54
Chu, C.-Y., & Chang, H.-K. 2023, MNRAS, 526, 1287
Collazzi, A. C., Kouveliotou, C., van der Horst, A. J., et al. 2015, ApJS, 218, 11
Coti Zelati, F., Rea, N., Pons, J. A., Campana, S., & Esposito, P. 2018, MNRAS, 474, 961
Dong, F. A. & Chime/Frb Collaboration 2022, ATel, 15681, 1
Duncan, R. C., & Thompson, C. 1992, ApJL, 392, L9
Enoto, T., Ng, M., Hu, C.-P., et al. 2021, ApJL, 920, L4
Gavriil, F. P., Gonzalez, M. E., Gotthelf, E. V., et al. 2008, Sci, 319, 1802
Gavriil, F. P., Kaspi, V. M., & Woods, P. M. 2002, Natur, 419, 142
Geminardi, A., Esposito, P., Bernardi, G., et al. 2025, A&A, 700, A19
Gendreau, K. C., Arzoumanian, Z., Adkins, P. W., et al. 2016, SPIE, 9905, 99051H
Giri, U., Andersen, B. C., Chawla, P., et al. 2023, arXiv:2310.16932
Göğüş, E., Kouveliotou, C., Woods, P. M., et al. 2001, ApJ, 558, 228
Göğüş, E., Lin, L., Kaneko, Y., et al. 2016, ApJL, 829, L25
Güver, T., Göğüş, E., Vurgun, E., et al. 2019, ApJL, 877, L30
Guver, T., Hu, C.-P., Younes, G., et al. 2021, ATel, 14916, 1
Hu, C.-P., Begiçarslan, B., Güver, T., et al. 2020, ApJ, 902, 1
Hu, C.-P., Kuiper, L., Harding, A. K., et al. 2023, ApJ, 952, 120
Hu, C.-P., Narita, T., Enoto, T., et al. 2024, Natur, 626, 500
Hu, C.-P., Wadiasingh, Z., Ho, W. C. G., et al. 2025, ApJ, 989, 63
Israel, G. L., Burgay, M., Rea, N., et al. 2021, ApJ, 907, 7
Israel, G. L., Romano, P., Mangano, V., et al. 2008, ApJ, 685, 1114
Jahoda, K., Markwardt, C. B., Radeva, Y., et al. 2006, ApJS, 163, 401
Kırmizibayrak, D., Şaşmaz Muş, S., Kaneko, Y., & Göğüş, E. 2017, ApJS, 232, 17
Kirsten, F., Snelders, M. P., Jenkins, M., et al. 2021, NatAs, 5, 414
Kouveliotou, C., Meegan, C. A., Fishman, G. J., et al. 1993, ApJL, 413, L101
Lamb, R. C., Fox, D. W., Macomb, D. J., & Prince, T. A. 2002, ApJL, 574, L29
Li, C. K., Lin, L., Xiong, S. L., et al. 2021, NatAs, 5, 378
Liang, E. P., & Antiochos, S. K. 1984, Natur, 310, 121
Lin, L., Göğüs, E., Kaneko, Y., & Kouveliotou, C. 2013, ApJ, 778, 105
Mazets, E. P., Golenetskij, S. V., & Guryan, Y. A. 1979a, SvAL, 5, 343
Mazets, E. P., Golentskii, S. V., Ilinskii, V. N., Aptekar, R. L., & Guryan, I. A. 1979b, Natur, 282, 587
Mereghetti, S., Savchenko, V., Ferrigno, C., et al. 2020, ApJL, 898, L29
Merloni, A., Lamer, G., Liu, T., et al. 2024, A&A, 682, A34
Meszaros, P. 1992, High-energy Radiation from Magnetized Neutron Stars (Univ. Chicago Press)
Nasa High Energy Astrophysics Science Archive Research Center (HEASARC) 2014, HEAsoft: Unified Release of FTOOLS and XANADU, Astrophysics Source Code Library, ascl:1408.004
Olausen, S. A., & Kaspi, V. M. 2014, ApJS, 212, 6
Pacholski, D. P., Mereghetti, S., & Topinka, M. 2026, ApJ, 997, 272
Paczynski, B. 1992, AcA, 42, 145
Remillard, R. A., Loewenstein, M., Steiner, J. F., et al. 2022, AJ, 163, 130
Scargle, J. D. 1998, ApJ, 504, 405
Scargle, J. D., Norris, J. P., Jackson, B., & Chiang, J. 2013, ApJ, 764, 167
Thompson, C., & Duncan, R. C. 1995, MNRAS, 275, 255
Tiengo, A., Vianello, G., Esposito, P., et al. 2010, ApJ, 710, 227
van der Horst, A. J., Kouveliotou, C., Gorgone, N. M., et al. 2012, ApJ, 749, 122
Wang, C.-W., Xiong, S.-L., Wang, Y., et al. 2026, MNRAS, 546, stag312
Younes, G., Baring, M. G., Kouveliotou, C., et al. 2021, NatAs, 5, 408
Younes, G., Güver, T., Kouveliotou, C., et al. 2020, ApJL, 904, L21
Younes, G., Hu, C.-P., Bansal, K., et al. 2022, ApJ, 924, 136
Younes, G., Lander, S. K., Baring, M. G., et al. 2025, ApJ, 989, 89